


Research Article

The radio properties of quasi-periodic X-ray eruption sources

Adelle Jane Goodwin¹, Riccardo Arcodia², Giovanni Miniutti³, James Carl Alexander Miller-Jones¹ and Sjoert van Velzen⁴

¹International Centre for Radio Astronomy Research, Curtin University, Perth, WA, Australia, ²Kavli Institute for Astrophysics and Space Research, Massachusetts Institute of Technology, Cambridge, MA, USA, ³Centro de Astrobiología (CAB), CSIC-INTA, Villanueva de la Cañada, Madrid, Spain and ⁴Leiden Observatory, Leiden University, RA Leiden, The Netherlands

Abstract

Quasi-periodic X-ray eruptions (QPEs) are a new class of repeating nuclear transient in which repeating X-ray flares are observed coming from the nuclei of generally low-mass galaxies. Here, we present a comprehensive summary of the radio properties of 12 bona-fide quasi-periodic eruption sources, including a mix of known tidal disruption events (TDEs) and AGN-like hosts. We include a combination of new dedicated radio observations and archival/previously published radio observations to compile a catalogue of radio observations of each source in the sample. We examine the overall radio properties of the sample and compare to the radio properties of known TDEs, given the apparent link between QPEs and TDEs. Overall we find compact, weak radio sources associated with 5/12 of the QPE sources and no signatures of strong AGN activity via a luminous radio jet. We find no radio variability on hour- to day-timescales corresponding to the X-ray QPEs, but do detect significant changes over year timescales in some sources, implying that the mechanism that produces the X-ray flares does not generate strong radio-emitting outflows. The compactness of the radio sources and lack of correlation between radio luminosity and SMBH mass is very unusual for AGN, but the radio spectra and luminosities are consistent with outflows produced by a recent TDE (or accretion event), in both the known TDE sources and the AGN-like sources in the sample.

Keywords: Accretion; accretion discs; galaxies: active; radio continuum: general

(Received 17 June 2025; revised 29 July 2025; accepted 12 August 2025)

1. Introduction

Quasi-periodic X-ray eruptions (QPEs) are a newly discovered type of X-ray transient that are characterised by fast and repeating quasi-periodic soft X-ray bursts emitted from the nuclei of low-mass galaxies. They show an X-ray flux increase of more than one order of magnitude over the quiescent plateau with durations of minutes to hours. To date, 12 QPE emitting galaxies have been discovered: GSN 069 (Miniutti et al. 2019), RX J1301.9+2747 (Giustini, Miniutti, & Saxton 2020), eRO-QPE1 (Arcodia et al. 2021), eRO-QPE2 (Arcodia et al. 2021), eRO-QPE3 (Arcodia et al. 2024a), eRO-QPE4 (Arcodia et al. 2024a), eRO-QPE5 (Arcodia et al. 2025), XMMSLJ024916.6–041244 (Chakraborty et al. 2021, J0249;), ZTF19acnskyy (Ansky; Hernández-García et al. 2025), and the optically selected tidal disruption events (TDEs) AT2019qiz (Nicholl et al. 2024), AT2022upj (Chakraborty et al. 2025a), and AT02019vcb (Quintin et al. 2023; Bykov et al. 2025). The recurrence time for these sources varies from hours to up several days, and all show a remarkably identical spectral evolution over time during the bursts (e.g. Arcodia et al. 2022; Miniutti et al. 2023).

The physical mechanism that produces QPEs has been proposed to be broadly due to either disc instabilities or interactions between the central SMBH and/or its accretion disc in an extreme mass ratio inspiral (EMRI). In the accretion disc instability

scenario, the flares could be due to either instabilities propagating through the disc (Sniegowska et al. 2020; Pan et al. 2022; Kaur, Stone, & Gilbaum 2023) or disc tearing due to disc warping effects (Raj & Nixon 2021). In the EMRI models, scenarios involving a two-body system consisting of a massive black hole and an orbiting companion with much smaller mass (e.g. King 2020; Zhao et al. 2022; Wang et al. 2022; Linial & Sari 2023), or scenarios in which an orbiting companion undergoing an EMRI passes through a compact pre-existing accretion disc (Arcodia et al. 2021; Suková et al. 2021; Linial & Metzger 2023) have been proposed. In the latter scenario, the orbiting body interacts with and shocks the gas in the accretion disc twice on each orbit, which seems to reproduce the observational properties (including the quasi-periodicity of the observed X-ray flares) qualitatively (Lu & Quataert 2023; Linial & Metzger 2023; Franchini et al. 2023). In some of these EMRI models, the accretion disc is remaining from a relatively recent TDE (e.g. Linial & Metzger 2023). More recently, Yao et al. (2025) showed that repeated star-disc collisions would result in increasing mass loss each collision, suggesting that QPEs are not powered from direct star-disc collisions but instead from stellar debris collisions with the accretion disc. Mummery (2025) showed that star-disc collisions with realistic TDE disc models cannot replicate observed QPE flare luminosities, durations, temperatures, and energies, but that a model that invokes stellar debris stream collisions may.

The connection between QPEs and TDEs was strengthened by the detection of QPEs in the optically discovered TDEs AT2019qiz (Nicholl et al. 2024), AT2022upj (Chakraborty et al. 2025a), and AT2019vcb (Quintin et al. 2023; Bykov et al. 2025). Additionally,

Corresponding author: Adelle Jane Goodwin; Email: adelle.goodwin@curtin.edu.au

Cite this article: Goodwin AJ, Arcodia R, Miniutti G, Miller-Jones JCA and van Velzen S. (2025) The radio properties of quasi-periodic X-ray eruption sources. *Publications of the Astronomical Society of Australia* 42, e130, 1–11. <https://doi.org/10.1017/pasa.2025.10083>

© The Author(s), 2025. Published by Cambridge University Press on behalf of Astronomical Society of Australia. This is an Open Access article, distributed under the terms of the Creative Commons Attribution licence (<https://creativecommons.org/licenses/by/4.0/>), which permits unrestricted re-use, distribution and reproduction, provided the original article is properly cited.

other QPE sources have shown TDE-like observational properties. Decade-long monitoring of GSN 069 has shown a long-term X-ray decay including a re-brightening that has been suggested to be due to a partial TDE (Miniutti et al. 2023), eRO-QPE3 shows a long term X-ray decay (Arcodia et al. 2024a) and the QPE candidate in Chakraborty et al. (2021) showed a TDE-like multi-wavelength flare prior to the discovery of X-ray variability.

Little is currently known about the radio properties of QPE sources, except for radio detections of GSN 069 presented in Miniutti et al. (2019) and Rx J1302 presented in Shu et al. (2017), Yang et al. (2022), and Giustini et al. (2024). This is due to the fact that to date not all sources have been observed in the radio, and not all sources were detected if they were observed. TDEs have been found to produce extremely diverse radio emission properties that are well described by outflows ejected by the stellar disruption or accretion process (Alexander et al. 2020). Some radio outflows appear as highly collimated relativistic jets (e.g. Zauderer et al. 2011; Pasham et al. 2023), whilst others present slower-moving, likely quasi-spherical outflows (e.g. Alexander et al. 2016; van Velzen et al. 2016; Goodwin et al. 2022). The radio emission from TDEs evolves on timescales of months (e.g. Goodwin et al. 2024; Goodwin et al. 2023a; Goodwin et al. 2023b; Alexander et al. 2016) and in some cases can be delayed by up to years post TDE (e.g. Cendes et al. 2022). However, not all TDEs produce detectable radio emission, with current observations indicating approximately 50% of events seem to produce detectable radio emission within ~ 5 yr of the TDE (Alexander et al. 2020; Cendes et al. 2024; Goodwin et al. 2025). Given the strengthening link between TDEs and QPEs, it may be expected that QPE sources exhibit similar radio properties to TDEs.

In this work, we present a comprehensive summary of the radio properties of 12 bona-fide QPE sources. We include a combination of new dedicated radio observations and archival/previously published radio observations to examine the overall radio properties of these sources and compare to the radio properties of known TDEs. In Section 2, we present the sample selection and radio observations available for each source, in Section 3 we summarise the radio lightcurves, spectra, and variability statistics for each source, in Section 4 we search for any correlations between radio emission and QPE flare and host properties, in Section 5 we discuss the implications of these results in the context of interpreting the physical mechanism of QPEs, and finally in Section 6 we summarise the results and provide concluding remarks.

2. Sample selection and radio observations

We searched the literature for confirmed QPE sources. This search resulted in 12 bona-fide QPE sources (where we define ‘bona-fide’ as a source having two or more QPE flares observed with QPE-like spectral evolution, i.e. a harder rise than decay), with flare recurrence times of 2–122 h. The 12 sources in our sample and their key properties are listed in Table 1.

Of the 12 sources, 8 have radio observations previously published in the literature, we obtained dedicated follow-up radio observations of 3 (including additional radio observations of GSN 069 to constrain any long-term variability), and we searched archival radio survey data for the remaining 2. A summary of all of the radio observations available for each of the sources is given in the online Appendix in Table B1.

2.1 New radio observations

2.1.1 ATCA

We obtained dedicated radio observations with the Australia Compact Telescope Array (ATCA) of eRO-QPE2 and GSN 069. We observed the coordinates of eRO-QPE2 on three occasions at central frequencies of 2.1, 5.5, and 9 GHz and the coordinates of GSN 069 on one occasion at a central frequency of 2.1, 5.5, and 9 GHz. In all observations, we used the full 2.048 GHz of bandwidth split into 2048 spectral channels. All radio observations were reduced using standard procedures in the Common Astronomy Software Application (CASA; CASA Team et al. 2022), including flux calibration with PKS 1934–638 and phase calibration with PKS 0244–470 (eRO-QPE2) and PKS 0104–408 (GSN069). Images of the target field were created using the CASA task `tclean` and source flux densities were extracted using the CASA task `imfit` by fitting a Gaussian the size of the synthesised beam. Reported flux densities include the statistical error from `imfit` and a systematic uncertainty estimated to be 5%, added in quadrature.

GSN 069 was detected at 2.1, 5.5, and 9 GHz and showed a point source coincident with nucleus of the host galaxy (Figure 1). eRO-QPE2 was detected at 5.5 and 9 GHz in the initial observation; however, due to the array being in the compact H214 configuration, it was confused with a nearby source (see Appendix A). We therefore report the measured flux densities for this epoch in Table B1 as an upper limit on the flux density of the target. In the second ATCA observation with the array in the extended 6 km configuration, eRO-QPE2 was marginally detected at 5.5 and 9 GHz and not detected at 2.1 GHz and did not suffer from confusion with the nearby radio sources. The radio source is consistent with a point source localised to the nucleus of the host galaxy (Figure 1). In the third ATCA observation, eRO-QPE2 was undetected, but the 3σ upper limit measured is consistent with the flux density measured in the second epoch. We conclude that there is a weak, compact radio source associated with eRO-QPE2, but we are unable to constrain any variability of the radio source associated with these observations.

2.1.2 VLA

AT2019vcb was observed by the Karl G. Jansky Very Large Array (VLA) in 2020 as part of a dedicated TDE radio follow-up program (program ID 20A-392). The source was observed four times between April 2020 and July 2020 at 2–15 GHz (S-, C-, X-, and Ku-band). In all observations, 3C286 was used for flux and bandpass calibration, and J1221+2813 (S-, C-, X-band) and J1310+3220 (Ku-band) were used for phase calibration. We reduced the data in CASA using standard procedures including the VLA pipeline. Images of the target field were created using the CASA task `tclean` and when a point source was detected at the location of the target, we used the CASA task `imfit` to fit a Gaussian the size of the synthesised beam in order to extract the flux density. Reported flux densities include the statistical error from `imfit` and a systematic uncertainty estimated to be 5%, added in quadrature. A faint, point-like radio source was detected in all observations except at 10 and 15 GHz in July 2020. The radio flux densities and 3σ upper limits are reported in Table B1.

2.1.3 Archival observations

We searched the VLA Sky Survey (VLASS; Lacy et al. 2020) for observations at the coordinates of the two sources in our

Table 1. A summary of the properties of the QPE sources studied in this work.

Source	z	t_{durQPE} (ks)	$t_{recurQPE}$ (ks)	$\log_{10} E_{QPE}$ (erg)	$\log_{10} M_{SMBH}$ (M_{\odot})*	$\log_{10} M_{gal}$ (M_{\odot})	SFR (M_{\odot}/yr)	$\log_{10} L_{5.5\text{ GHz},pk}$ (erg/s)	Ref.
GSN 069	0.018	4.50 ± 0.60	29.90 ± 9.50	46.11 ± 0.11	6.28 ± 0.72	–	–	36.34 ± 0.07	Miniutti et al. (2019); Miniutti et al. (2023)
Rx J1302	0.024	2.50 ± 1.10	12.90 ± 10.40	45.69 ± 0.21	6.14 ± 0.88	–	–	37.441 ± 0.003	Giustini et al. (2020); Giustini et al. (2024)
eRO-QPE1	0.051	26.60 ± 5.20	77.50 ± 27.00	48.08 ± 0.12	5.90 ± 0.79	9.58 ± 0.23	0.01 ± 0.00	< 36.99	Arcodia et al. (2021); Arcodia et al. (2022); Chakraborty et al. (2024)
eRO-QPE2	0.018	1.70 ± 0.10	8.30 ± 0.80	45.77 ± 0.04	5.43 ± 0.79	9.00 ± 0.21	0.08 ± 0.07	36.87 ± 0.06	Arcodia et al. (2021); Arcodia et al. (2024b)
eRO-QPE3	0.024	8.40 ± 0.45	72.00 ± 7.10	45.83 ± 0.13	5.53 ± 0.79	9.41 ± 0.24	0.20 ± 0.14	< 36.59	Arcodia et al. (2024a)
eRO-QPE4	0.044	3.60 ± 0.40	50.80 ± 10.10	46.46 ± 0.21	7.31 ± 0.75	10.20 ± 0.19	2.26 ± 2.20	< 37.11	Arcodia et al. (2024a)
eRO-QPE5	0.116	51.84 ± 9.50	319.68 ± 1.73	47.53 ± 0.09	7.45 ± 0.52	9.95 ± 0.18	–	< 37.86	Arcodia et al. (in prep)
AT2019qiz	0.015	31.90 ± 1.60	175.80 ± 19.40	47.68 ± 0.04	6.27 ± 0.76	10.26 ± 0.03	0.00 ± 3.50	37.33 ± 0.02	Nicholl et al. (2024)
ZTF19acnsky	0.024	125.50 ± 14.10	440.90 ± 85.20	47.99 ± 0.17	6.34 ± 0.66	–	–	< 36.81	Hernández-García et al. (2025); Sánchez-Sáez et al. (2024)
AT2022upj	0.054	59.00 ± 8.60	172.20 ± 54.20	47.77 ± 0.12	6.38 ± 0.56	9.59 ± 0.11	–	< 37.96	Chakraborty et al. (2025a); Newsome et al. (2024)
J0249	0.019	1.20 ± 0.05	9.50 ± 1.00	45.36 ± 0.12	5.00 ± 0.50	9.10 ± 0.17	–	< 37.02	Chakraborty et al. (2021); Wevers et al. (2019)
AT2019vcb	0.088	54 ± 18	144 ± 108	48.81 ± 0.15	6.81 ± 0.13	9.49 ± 0.06	–	37.5 ± 0.2	Quintin et al. (2023); Bykov et al. (2025)

*SMBH mass measurements are taken from Arcodia et al. (2025) where they have been averaged from various methods, including scaling with stellar mass (eRO-QPE3, eRO-QPE4, ZTF19acnsky, AT2022upj, J0249), velocity dispersion (AT2019qiz, J0249), and SED fitting (GSN 069, RxJ1302, AT2022upj, AT2019vcb).

z is the source redshift, t_{durQPE} is the average duration of the observed QPEs, $t_{recurQPE}$ is the average recurrence time of the QPEs, E_{QPE} is the average energy radiated per QPE, M_{SMBH} is the SMBH mass, M_{gal} is the galaxy stellar mass, SFR is the estimated star formation rate of the galaxy from SED fitting, and $L_{5.5\text{ GHz},pk}$ is the peak observed 5.5 GHz radio luminosity.

sample without dedicated radio observations available: AT2022upj and J0249. There were 2–3 epochs of VLASS observations available for each source, taken between 2017 and 2023. No radio source was detected coincident with the coordinates of either source in any of the VLASS observations. The 3σ VLASS upper limits are reported in Table B1.

We additionally searched the Rapid ASKAP Continuum Survey (RACS McConnell et al. 2020) for observations at the coordinates of each of the sources in the sample. All sources were undetected in publicly available RACS observations (with an average image rms of 300–400 μ Jy) except RX J1301.9+2747, for which a point source was detected in a 0.88 GHz RACS observation taken on 17 December 2020. The flux density of this observation is reported in Table B1.

3. Results

Five out of 12 of the QPE sources are radio-detected. The radio-detected sources are faint point-like sources and span a range of luminosities ($\nu L_{\nu} \sim 5 \times 10^{36} - 5 \times 10^{38}$ erg/s).

The radio contours of eRO-QPE2, GSN069, RXJ1302, and AT2019vcb are plotted over the Legacy Survey DR8–10 (Dey et al. 2019) optical images of the host galaxies in Figure 1. A publicly available image of the AT2019qiz radio observations was not available. It is clear that the radio sources are associated with the nucleus of each of the galaxies and are not consistent with diffuse star formation emission in the disc of the galaxies. Although, we cannot rule out faint radio emission from diffuse star formation emission in any of the observations due to the sensitivity of

the radio interferometers to faint diffuse emission on these length scales.

3.1 Radio lightcurves

The 5–6 GHz radio lightcurves of the five radio-detected QPE sources are plotted in Figure 2. AT2019qiz shows rising radio emission over ≈ 100 d and eRO-QPE2 and AT2019vcb show fading radio emission over a few hundred days, although the first observation of eRO-QPE2 is affected by a confusing source nearby. GSN 069 and RxJ1302 show approximately stable radio sources over ~ 1000 d. Previous studies have detected low-amplitude radio variability in GSN 069 (Miniutti et al. 2019) and Rx J1302 (Shu et al. 2017; Yang et al. 2022; Giustini et al. 2024), although no correlation with the X-ray QPE flares was observed.

3.2 Radio spectra

We plot the 1–20 GHz radio spectra of the five radio-detected sources in Figure 3. We fit each of the spectra with a simple power-law model:

$$F_{\nu} = A\nu^{\alpha} \quad (1)$$

where A is a normalisation constant and α is the spectral index. The measured spectral indices for each of the four sources are shown in Figure 3.

AT2019qiz shows an inverted radio spectrum typical of a young TDE that is evolving quickly as the radio spectral peak shifts down in frequency due to the expanding synchrotron-emitting region.

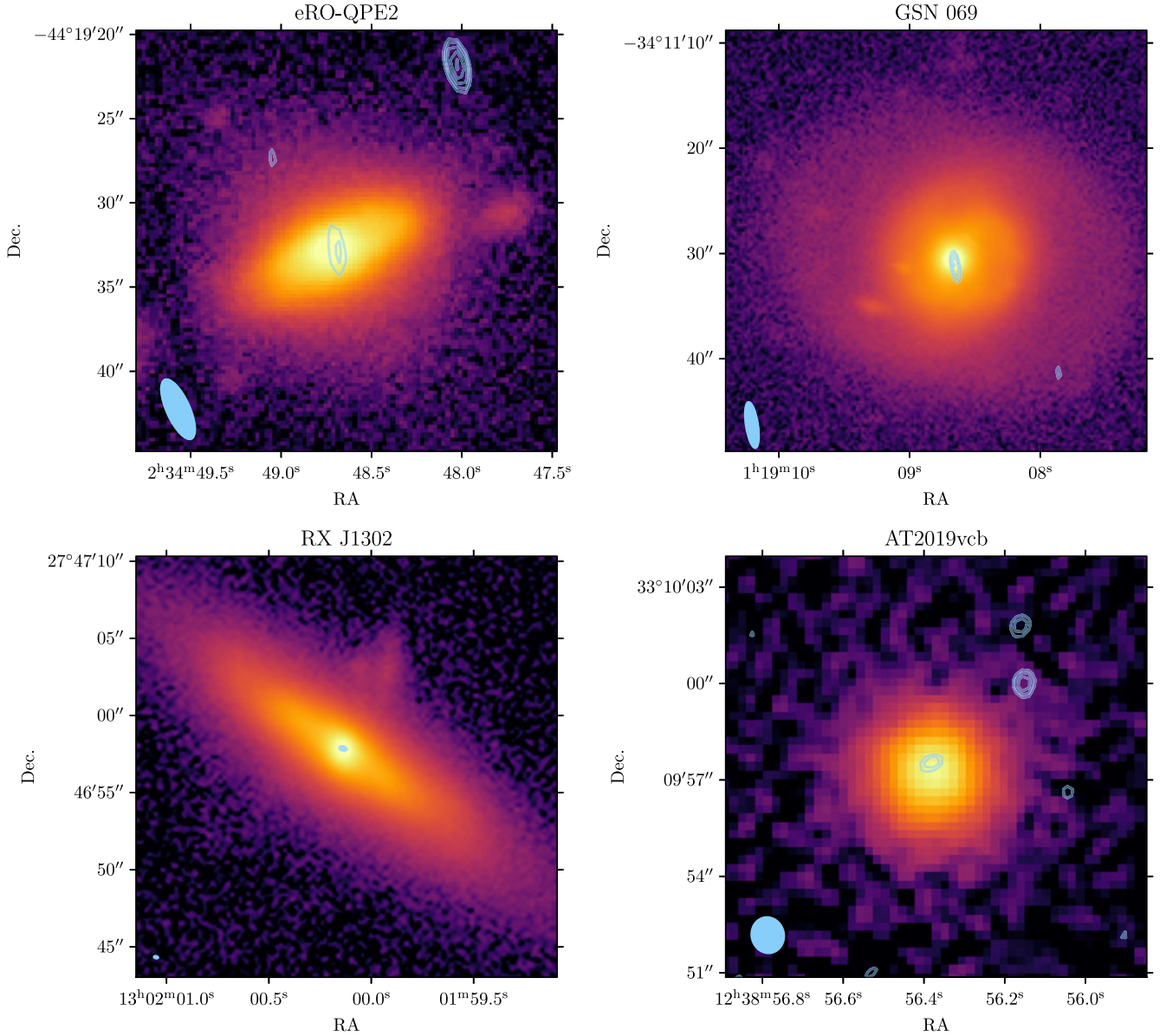


Figure 1. The DESI Legacy Survey DR8-DR10 optical images (Dey et al. 2019) of the host galaxies of eRO-QPE2, GSN 069, RX J1302, and AT2019vcb. The ATCA 5.5 GHz (eRO-QPE2 and GSN 069) and VLA 6 GHz (RX J1302 and AT2019vcb) radio contours are overlaid in blue, with the radio beam size indicated in the bottom left corner. The radio sources are all compact and localised to the nuclei of the host galaxies.

The remaining four sources show optically thin spectra with spectral indices in the range -0.7 to -0.9 , typical of host galaxy emission from star formation (e.g. Murphy et al. 2011), low luminosity AGN (e.g. Ho & Ulvestad 2001), or radio-emitting TDEs (e.g. Goodwin et al. 2025).

3.2.1 Equipartition analysis

Under the assumption that the spectra of the radio sources are described by an optically thin synchrotron source in which the peak of the emission is associated with synchrotron self-absorption, an equipartition analysis can be applied in order to place constraints on the physical properties of the synchrotron source. The majority of the sources shown in this work have spectral peaks below the observed bands, meaning only a lower limit on the equipartition radii and energies can be obtained.

The spectrum of a source in which the peak is associated with synchrotron self-absorption is given by Granot & Sari (2002):

$$F_{\nu,\text{synch}} = F_{\nu,\text{ext}} \left[\left(\frac{\nu}{\nu_a} \right)^{-s\beta_1} + \left(\frac{\nu}{\nu_a} \right)^{-s\beta_2} \right]^{-1/s} \quad (2)$$

where ν is the frequency, ν_a is the self-absorption frequency, $F_{\nu,\text{ext}}$ is the normalisation, $s = 1.25 - 0.18p$, $\beta_1 = \frac{5}{2}$, and $\beta_2 = \frac{1-p}{2}$.

The optically thin spectral index of a self-absorbed synchrotron source is therefore proportional to the synchrotron electron energy index, p via $\alpha = (1 - p)/2$ (e.g. Granot & Sari 2002). With the peak flux density, peak frequency, and p , we can then calculate an inferred minimum equipartition radius and energy for each of the QPE sources. To calculate the minimum radius and energy, we first assume the emitting region is approximately spherical

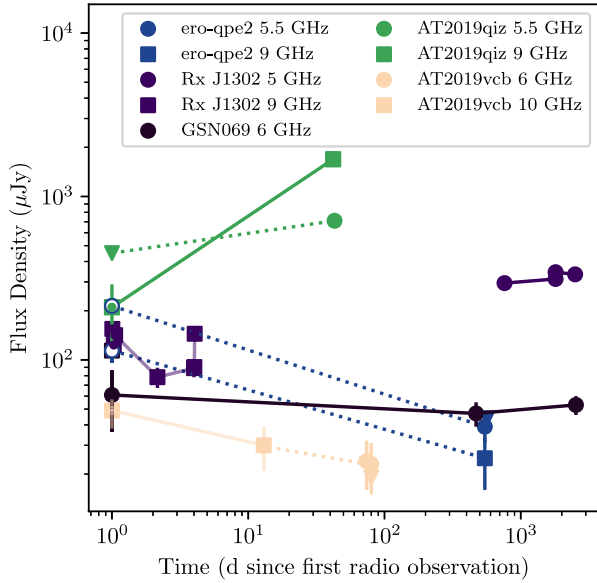


Figure 2. The 5–6 GHz (circles) and 10 GHz (squares) radio lightcurves of the five radio-detected QPE sources in our sample. Inverted triangles indicate 3σ upper limits and the open circle indicates the measured flux density affected by confusion with nearby sources. AT2019qiz and RxJ1302 show statistically significant radio variability, while GSN 069 is constant over the 5-yr baseline observed. AT2019vcb showed statistically significant variability at 10 GHz, but the two 6 GHz observations are only 6 d apart and do not show significant variability. Our observations of eRO-QPE2 are inconclusive regarding its radio variability (see Appendix A).

(with geometric factors^a $f_A = 1$ and $f_V = 4/3$). In the Newtonian regime, the equipartition energy, corresponding to the minimum total energy in the observed region, assuming $v_a > v_m$, is given by (Barniol Duran et al. 2013):

$$E_{\text{eq}} = 1.3 \times 10^{48} 21.8^{-\frac{2(p+1)}{13+2p}} (525^{(p-1)} \chi_e^{(2-p)})^{\frac{11}{13+2p}} F_{\text{peak, mJy}}^{\frac{14+3p}{13+2p}} \left(\frac{d}{10^{28} \text{ cm}} \right)^{\frac{2(3p+14)}{13+2p}} \left(\frac{v_{\text{peak}}}{10 \text{ GHz}} \right)^{-1} (1+z)^{-\frac{27+5p}{13+2p}} f_A^{-\frac{3(p+1)}{13+2p}} f_V^{-\frac{2(p+1)}{13+2p}} 4^{\frac{11}{13+2p}} \xi^{\frac{11}{13+2p}} \text{ erg}, \quad (3)$$

where d is the distance from the observer, z is the redshift, $\chi_e = \left(\frac{p-2}{p-1} \right) \epsilon_e \frac{m_p}{m_e}$ (m_e is the electron mass and m_p is the proton mass), or $\chi_e = 2$ if $\Gamma = 1$ (Newtonian case), and $\xi = 1 + \frac{1}{\epsilon_e}$.

The equipartition radius is given by:

$$R_{\text{eq}} = 1 \times 10^{17} (21.8(525^{(p-1)})^{\frac{1}{13+2p}} \chi_e^{\frac{2-p}{13+2p}} F_{\text{peak}}^{\frac{6+p}{13+2p}} \left(\frac{d}{10^{28} \text{ cm}} \right)^{\frac{2(p+6)}{13+2p}} \left(\frac{v_{\text{peak}}}{10 \text{ GHz}} \right)^{-1} (1+z)^{-\frac{19+3p}{13+2p}} f_A^{-\frac{5+p}{13+2p}} f_V^{-\frac{1}{13+2p}} 4^{\frac{1}{13+2p}} \xi^{\frac{1}{13+2p}} \text{ cm}. \quad (4)$$

Given the equipartition radius and energy, additional physical outflow parameters such as the magnetic field B , ambient electron density n_e , and the mass in the emitting region M_{em} can be inferred. For these physical quantities, we use the equations presented in Goodwin et al. (2022).

For all sources except AT2019qiz, the peak of the radio spectrum is below the observed band. For these sources, we therefore measure an upper bound on the peak frequency by taking the

^aThe geometric factors, defined in Barniol Duran et al. (2013), are given by $f_A = A/(\pi R^2/\Gamma^2)$ and $f_V = V/(\pi R^3/\Gamma^4)$, for an outflow with area, A , volume, V , and distance from the origin of the outflow, R .

lowest observed frequency and a lower bound on the peak flux density as the highest observed peak flux density. For AT2019qiz, the spectrum at 74 d post-TDE shows curvature that allows the synchrotron self-absorption frequency and peak flux density to be fit directly. We report the equipartition results in Table 2. Overall, we constrain the minimum radii of the QPE sources to be $< 2 \times 10^{17}$ cm, indicating a compact nature of the radio sources.

3.3 Radio variability statistics

In order to assess the radio variability properties of the radio-detected sources in our sample, we calculate a variability statistic for the sources in which multiple observations are available at the same observing frequency. We calculate a variability statistic, V , such that

$$V = \frac{(S_{\text{max}} - \sigma_{S_{\text{max}}}) - (S_{\text{min}} + \sigma_{S_{\text{min}}})}{(S_{\text{max}} - \sigma_{S_{\text{max}}}) + (S_{\text{min}} + \sigma_{S_{\text{min}}})}, \quad (5)$$

where S_{max} and S_{min} are the maximum and minimum observed flux density, and $\sigma_{S_{\text{max}}}$ and $\sigma_{S_{\text{min}}}$ are their associated uncertainties. Any value of $V > 0$ indicates statistically significant variability. The calculated values of V for each of the detected radio sources are given in Table 3.

GSN 069 does not show statistically significant variability over the 5-yr baseline probed, whereas RxJ1302, AT2019qiz, and AT2019vcb do show statistically significant variability. Our observations of eRO-QPE2 are inconclusive regarding its radio variability due to a confusing source in the first observation (see 7).

In comparison, the 5.5 and 9 GHz variability statistics of the X-ray selected TDE sample presented in Goodwin et al. (2025) range from 0.05 to > 0.6 , and the 4.8 GHz variability statistics of the AGN sample presented in Hovatta et al. (2008) range from 0.1 to 1. Therefore, the level of radio variability observed in the QPE sources is consistent with both TDE and AGN samples.

4. Search for correlations between radio emission and flare/host properties

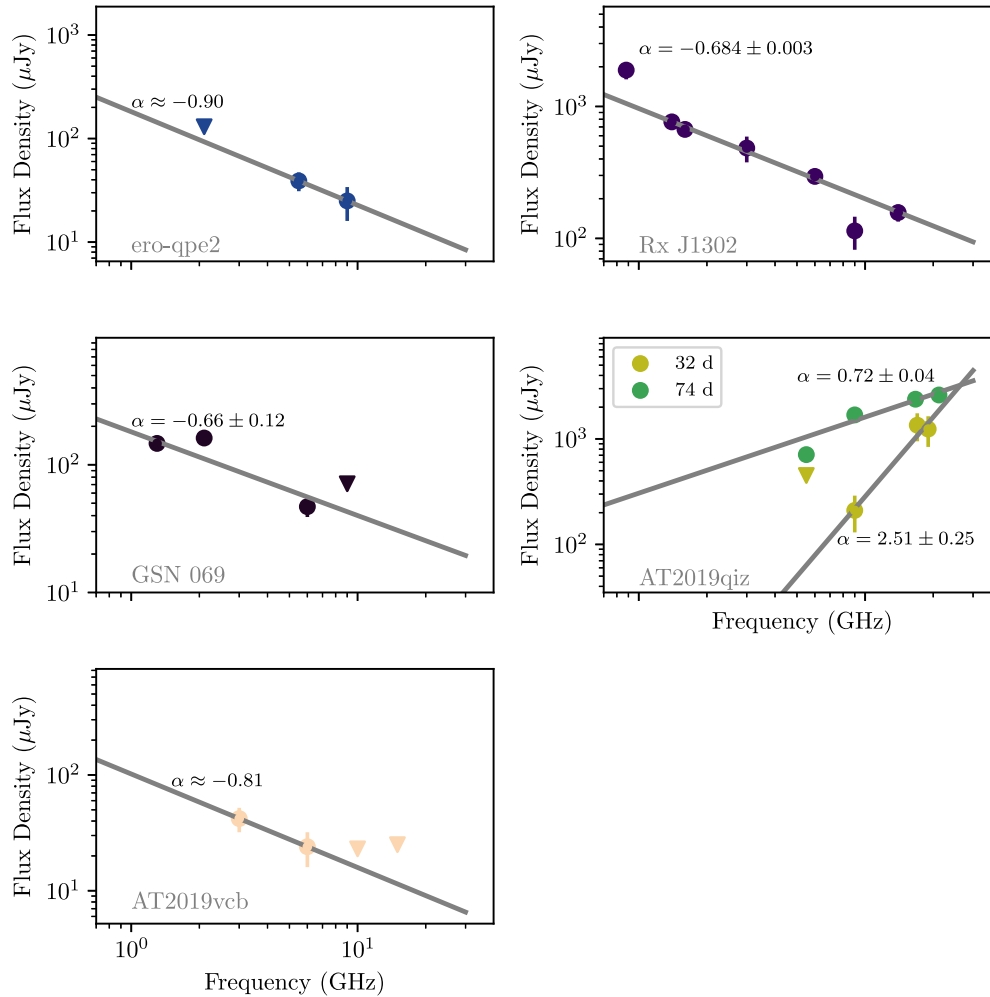
Given the radio sources associated with the five radio-detected QPE sources are compact and associated with the nuclei of the host galaxies (Figure 1), hinting that the radio emission could be due to the QPE mechanism or the mechanism that produced the accretion disc, here we search for any correlation between the measured radio luminosity of the QPE sources and their QPE flare and host properties.

A strong positive correlation between observed QPE X-ray flare duration (t_{dur}) and the average recurrence time (t_{recurr}) has previously been established (e.g. Arcodia et al. 2024a; Mummery 2025). In Figure 4, we plot each of the 12 QPE sources in our sample with the radio-detected sources indicated. In this figure, it is evident that the radio-detected QPE sources do not occupy the same region of $t_{\text{dur}}/t_{\text{recurr}}$ parameter space, implying that the radio luminosity is not directly linked to the QPE flare duration or recurrence time.

In Figure 5, we plot the observed peak 5.5 GHz radio luminosities against the observed 0.2–2 keV QPE and quiescent X-ray luminosities for each of the sources. No correlation between the radio luminosity and either of the X-ray luminosities is visually apparent, and a Pearson correlation test of the radio-detected sources returns a correlation coefficient of 0.58 and p -value of 0.30 (for QPE X-ray luminosity) and correlation coefficient of -0.65 and p -value of 0.23 (for quiescent X-ray luminosity). We therefore

Table 2. Physical outflow properties obtained via equipartition analysis of the radio-detected QPE sources.

Source	F_p (mJy)	ν_p (GHz)	ρ	R (cm)	E (erg)	B (G)	n_e (cm $^{-3}$)	M_{em} (M_{\odot})
GSN 069	> 0.16	< 1.3	2.3	$> 2.24 \times 10^{16}$	$< 9.58 \times 10^{46}$	< 0.13	< 71	$< 1.33 \times 10^{-7}$
Rx J1302	> 1.89	< 0.88	2.4	$> 1.38 \times 10^{17}$	$< 5.64 \times 10^{48}$	< 0.07	< 17.7	$< 6.55 \times 10^{-6}$
eRO-QPE2	> 0.039	< 5.5	2.8	$> 2.9 \times 10^{15}$	$< 1.07 \times 10^{46}$	< 0.94	< 3495	$< 4.15 \times 10^{-8}$
AT2019qiz	4.6 ± 0.4	10.8 ± 0.6	2.3 ± 0.3	$1.04 \pm 0.65 \times 10^{16}$	$4.18 \pm 0.45 \times 10^{47}$	0.6 ± 0.2	4150 ± 2061	$7.3 \pm 0.9 \times 10^{-7}$
AT2019vcb	> 0.042	< 3	2.6	$> 2.3 \times 10^{16}$	$< 6.6 \times 10^{47}$	< 0.33	< 452	$< 9.04 \times 10^{-7}$

**Figure 3.** Radio spectra of the five radio-detected QPE sources. In each plot, the solid line shows the simple power-law model used to constrain the spectral index, α , for each source, where $F_{\nu} \propto \nu^{\alpha}$. Inverted triangles indicate 3σ upper limits. For AT2019qiz, two spectra are plotted and labelled by days, since optical discovery of the TDE. We plot only the ATCA observation taken in December 2023 for eRO-QPE2.

do not find a statistically significant correlation between the QPE or quiescent X-ray luminosities and the radio luminosity of the QPE sources.

We further search for any correlation between QPE flare properties and radio emission by plotting the observed 5.5 GHz radio luminosity against QPE average energy radiated, duration, and recurrence time in Figure 6. We find no apparent correlation between radio luminosity and any of the QPE flare properties examined. Performing a Pearson correlation test for the radio-detected sources, we obtain coefficients of 0.5–0.62 with p-values

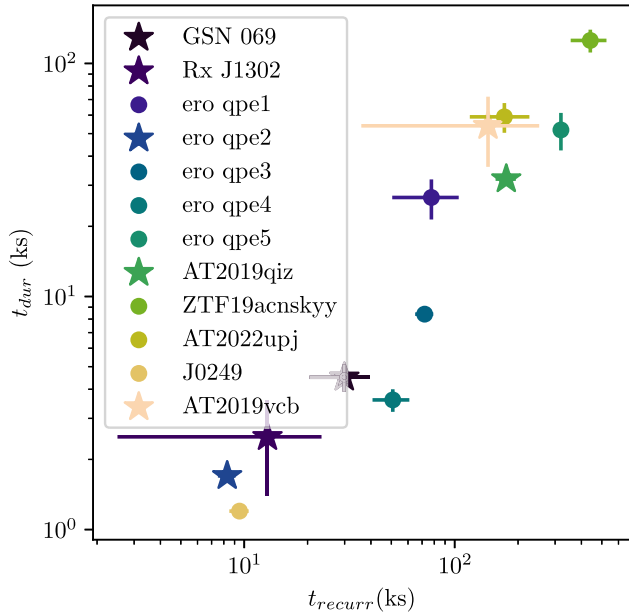
of 0.27–0.38, indicating no statistically significant linear correlation between the radio luminosities and QPE flare properties.

Next, we search for any correlation between the QPE host galaxy properties and the observed radio emission. In Figure 6, we plot the observed 5.5 GHz radio luminosity against QPE host SMBH mass, galaxy mass, and star formation rate (where these properties were available in the literature for each source). We find no apparent correlation between radio luminosity and any of the QPE host properties examined. Performing a Pearson correlation test for the radio-detected sources, we obtain coefficients of

Table 3. The variability statistic, V , of the radio emission from each of the radio-detected sources in the sample.

Source name	Obs. Freq. (GHz)	V	Variable?
GSN 069	6	-0.21	No
RX J1301.9+2747	5	0.06	Yes
	9	0.23	Yes
eRO-QPE2	5.5	<0.61	Unsure*
AT2019qiz	5.5	0.70	Yes
AT2019vcb	10	>0.33	Yes

*The variability of this source observed may be due to resolution differences in the two observations and a nearby confusing source, see Appendix 1.

**Figure 4.** The QPE flare recurrence time (t_{recurr}) and flare duration (t_{dur}) for each of the 12 QPEs in our sample. Stars indicated QPE sources associated with a compact radio source, while circles indicate radio-undetected QPE sources. We find no correlation between the presence of radio emission and the duration or recurrence time of the QPEs.

0.25–0.56 with p -values of 0.32–0.68, indicating no statistically significant linear correlation between the radio luminosities and QPE host galaxy properties.

5. Discussion

Our findings reveal that over half (7/12) of the known QPE sources are not associated with radio sources. Of the 5/12 QPE sources associated with radio sources, the radio emission is faint for radio emission associated with the nuclei of galaxies ($\nu L_{\nu} \sim 5 \times 10^{36} - 5 \times 10^{38}$ erg/s) and localised to the nucleus of the galaxy (Figure 1).

5.1 The nature of the radio sources

Given the detected radio sources associated with five of the QPE sources are compact and low luminosity, they may be linked to either the QPE mechanism in the form of a persistent radio-emitting jet or outflow or synchrotron emission from expanding material ejected in each flare, or a compact jet or outflow due to low-level AGN or previous TDE activity. Radio emission from star formation in the host galaxies is an unlikely explanation for

the radio emission given the compactness of the radio sources. This conclusion is strengthened by the lack of correlation between radio luminosity and galaxy star formation rate in Figure 6.

The radio source associated with Rx J1302 has been studied the most extensively to date due to it having the highest flux density of the sources in the sample. Yang et al. (2022) showed in extensive VLA observations taken between 2015 and 2019 that there is significant variability of the radio source on timescales as short as days, implying an emission region size $< 10^{-3}$ pc if the variability is intrinsic to the source. VLBA observations at 1.6 GHz revealed compact radio emission unresolved on scales < 0.7 pc (Yang et al. 2022). Giustini et al. (2024) provided detailed radio monitoring observations of the source taken between 2020 and 2022 and found significant variability on timescales as short as hours; however, in simultaneous XMM-Newton and VLA observations of five QPE flares, there was no radio variability correlated with the QPEs. Yang et al. (2022) and Giustini et al. (2024) deduce that the stochastic radio variability is consistent with variability induced by interstellar scintillation if the source is < 0.008 pc. Such a small source size rules out star formation or pc-scale jets or outflows typically seen in AGN, leaving the possibility of a persistent compact jet, episodic jet ejections, or a compact outflow. Simultaneous MeerKAT and Chandra observations of GSN 069 reported by Miniutti et al. (2019) also showed no radio variability associated with the one QPE flare observed simultaneously, with correlated variability excluded down to the few percent level. In this work, we additionally find no statistically significant radio variability over a 5-yr baseline, despite the decade-long X-ray decay that has been observed in this source (e.g. Miniutti et al. 2023). In Section 4, we found no apparent correlation between the observed radio luminosities and the QPE flare properties (Figure 6). The lack of correlation between the QPE X-ray variability and radio variability rules out a common mechanism for the radio emission and QPE flares.

The alternative is that the radio emission is produced by black hole activity, which could take the form of low-level AGN jet activity or an old outflow from a TDE. Whilst AGN commonly have radio spectral indices in the range of those of our radio-detected sample (Ho & Ulvestad 2001), AGN are very rarely compact on linear scales < 1 kpc (e.g. Ho & Ulvestad 2001; Anderson & Ulvestad 2005). In our observations of eRO-QPE2 and GSN 069, based on the resolution we constrain the sources to be $< 2.3''$ and $< 5.6''$, respectively, corresponding to linear sizes of < 0.9 kpc and < 2.2 kpc at 9 GHz. VLBI observations of RxJ1302 constrained the source to be < 0.7 pc (Yang et al. 2022). In Section 3.2.1, we constrained the minimum equipartition radii of the QPE sources via their spectral peak to all be $< 2 \times 10^{17}$ cm (< 0.06 pc), further confirming the compact nature of the radio sources. Encountering 3/3 compact persistent radio-detected sources in our sample (excluding the TDEs AT2019qiz and AT2019vcb which show transient radio emission linked to the optical TDEs) would be very unlikely in a random sample of AGN, suggesting that the radio sources in this sample are unusual for AGN. There is a strong observational correlation between radio AGN activity and SMBH/galaxy mass (e.g. Best et al. 2005), which we do not observe in our sample (although with very low sample statistics). In Figure 6 there is no correlation between host galaxy properties, including SMBH mass, and the observed radio luminosities. Overall the compactness and lack of correlation with host properties of our radio-detected sources suggest the radio sources are either very unusual AGN or not AGN at all. This finding suggests the radio sources may

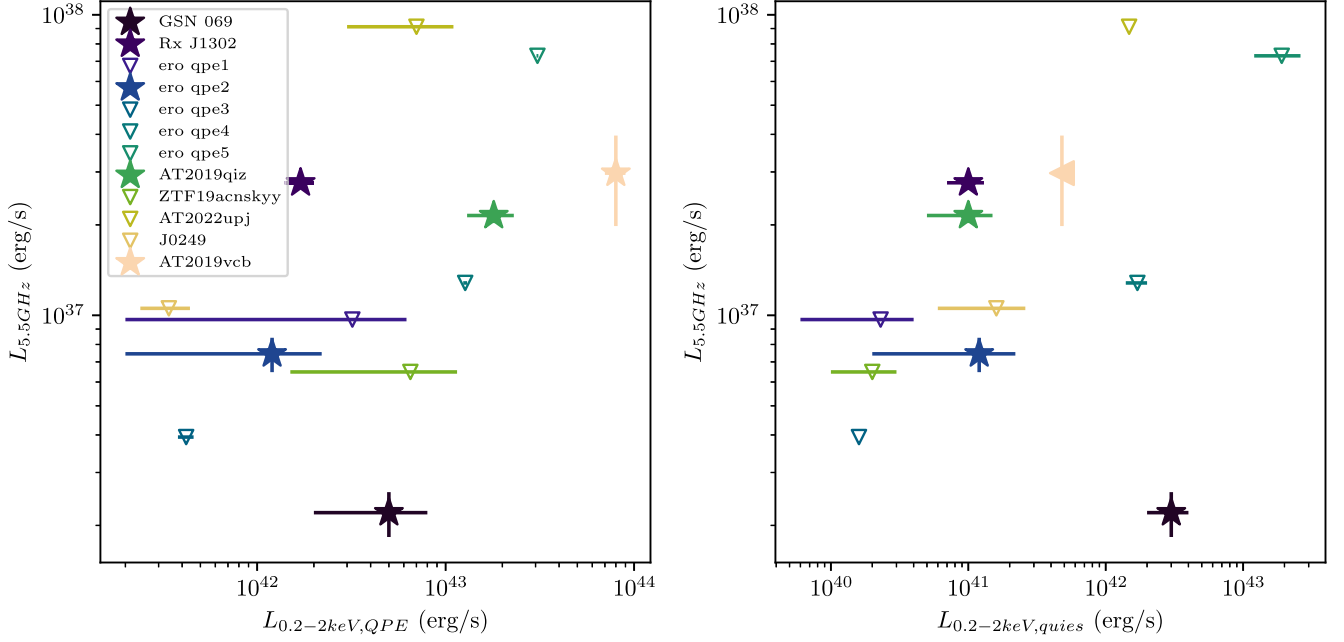


Figure 5. The QPE peak 0.2–2 keV X-ray luminosity (left panel) and quiescent 0.2–2 keV X-ray luminosity (right panel) plotted against 5.5 GHz radio luminosity for the 12 QPE sources in the sample. We find no statistically significant correlation between the radio and X-ray luminosities in the sample.

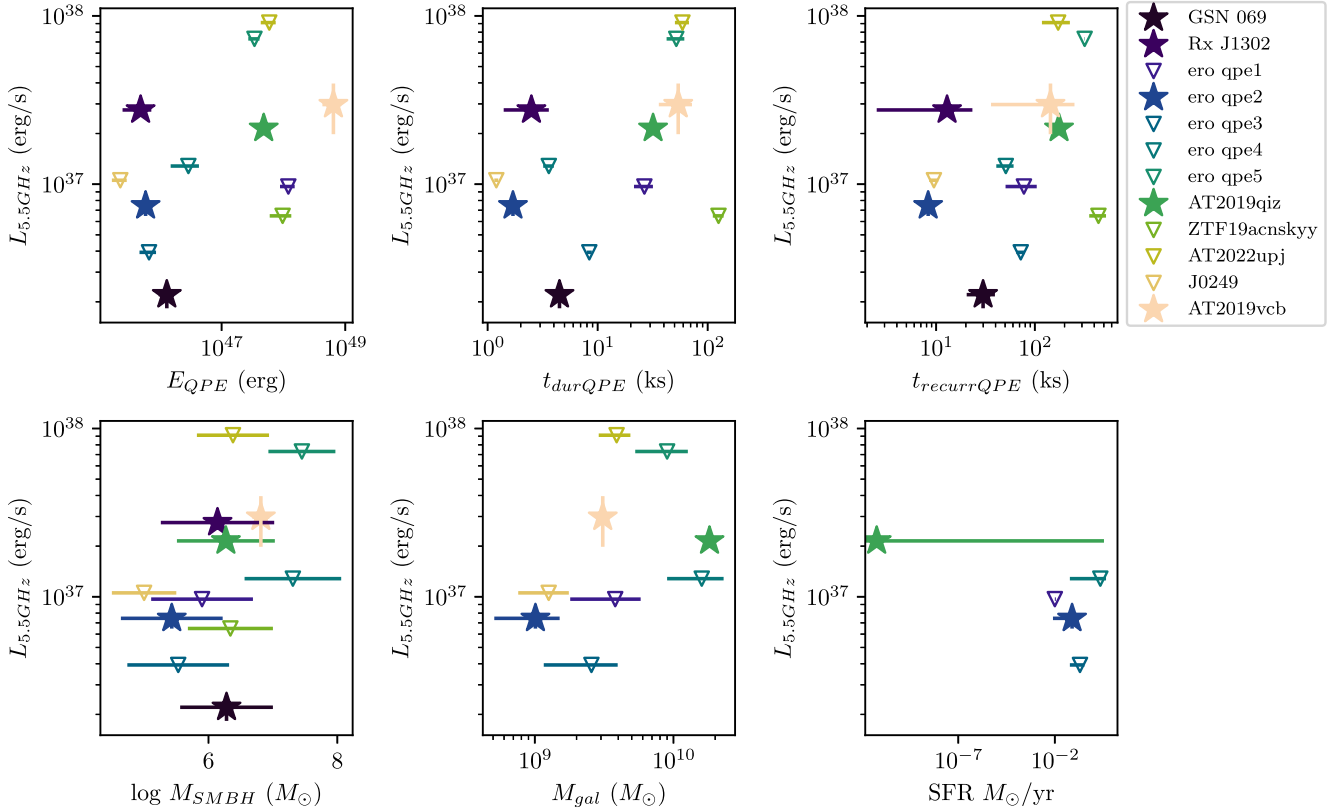


Figure 6. *Top row:* The QPE properties: total energy radiated, duration, and recurrence time plotted against the observed 5.5 GHz radio luminosity for the 12 QPEs in the sample. We find no correlation between radio luminosity and any of the QPE properties examined. *Bottom row:* The QPE host galaxy properties SMBH mass, galaxy mass, and star formation rate plotted against the observed 5.5 GHz radio luminosity for the 12 QPEs in the sample. Again we find no correlation between the radio luminosity and the host galaxy properties in our sample. Note that only five of the QPE sources had SFRs available in the literature.

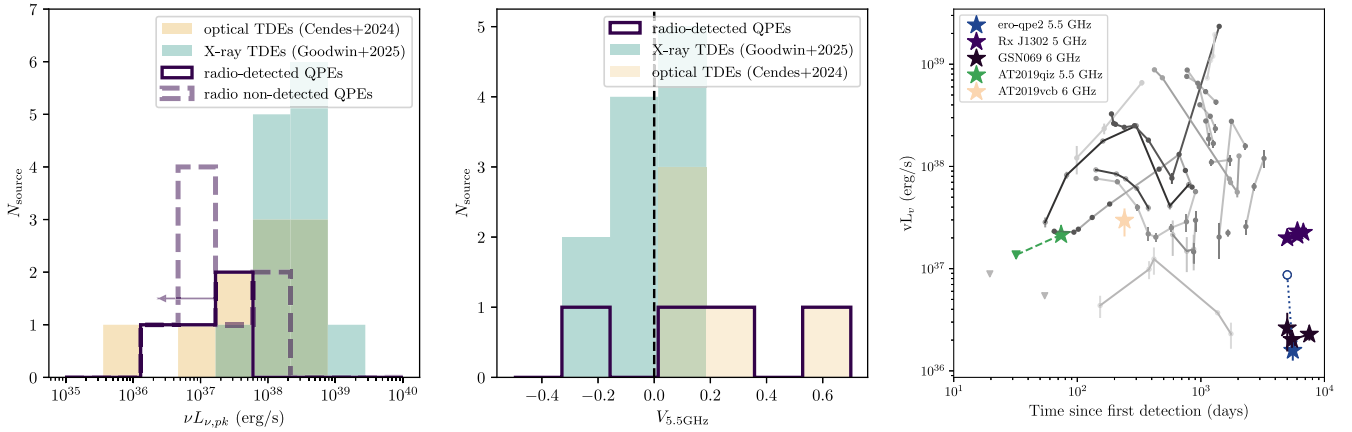


Figure 7. *Left:* The peak observed radio luminosity distribution of the radio-detected QPE sources (solid purple line) and upper limits (dashed purple line). For comparison, the peak observed radio luminosity distribution of the X-ray selected TDE population from Goodwin et al. (2025) is shown in blue and optically-selected TDE population from Cendes et al. (2024) is shown in yellow. The radio luminosity distribution of the QPE sources is broadly consistent with that of TDEs, albeit biased to slightly lower luminosities. *Middle:* The 5–6 GHz variability index ($V_{5.5GHz}$) for the radio-detected QPE sources, excluding eRO-QPE2 due to only an upper limit available (solid purple line). For comparison, the 5–6 GHz variability index of the X-ray selected TDE population from Goodwin et al. (2025) is shown in blue and optically selected TDE population from Cendes et al. (2024) is shown in yellow. Values above the dashed black line indicate statistically significant variability. *Right:* The observed radio lightcurve of known TDEs (grey) and the five radio-detected QPE sources. Note that eRO-QPE2, GSN 069, and RxJ1302 are scaled such that the first radio observation is plotted 5000 d after the first detection since the time the transient emission began is unconstrained. AT2019qiz and AT2019vcb are entirely consistent with the TDE population, while the remaining three QPE sources are less variable than TDEs, although the late-time radio behaviour of TDEs is unknown.

be produced by a more exotic mechanism, such as remnant TDE outflow emission or a compact jet. The lack of AGN features in QPE host galaxies is supported at optical wavelengths by a lack of broad emission lines in their optical spectra that is typical of unobscured AGN activity, although in some of the galaxies the narrow line ratios suggest an ionising source in excess of stars (e.g. Wevers et al. 2022, 2024).

5.2 Comparison to TDEs in the radio

The possibility that the radio sources are old synchrotron emitting regions from outflows produced by a TDE is particularly attractive given the apparent link between QPEs and TDEs (e.g. Nicholl et al. 2024; Miniutti et al. 2025; Bykov et al. 2025) and the disc-like quiescent emission observed in many QPE sources which is easily produced by a disc remaining from a previous TDE (e.g. Linial & Metzger 2023; Franchini et al. 2023). Recent studies of optical- and X-ray-selected samples of TDEs have found long-lived radio emission that can be rising up to 10 yr after the initial TDE (Cendes et al. 2024; Goodwin et al. 2025); however, the long-term (> 10 yr) radio emission behaviour of TDEs is unknown.

In Figure 7 (left), we plot the observed peak radio luminosity of two TDE samples (Cendes et al. 2024; Goodwin et al. 2025) and the luminosity distribution of the QPE sources. Broadly the luminosity range of the QPE sources is consistent with TDEs, noting that TDEs span a large range of observed peak luminosities. The radio detection rate of QPEs (42%) is consistent with typical radio detection rates of optical- and X-ray-selected TDEs (40–50% Cendes et al. 2024; Goodwin et al. 2025). In Figure 7 (right), we plot the observed radio lightcurves of the radio-detected QPE sources and those of known radio-emitting TDEs. AT2019qiz and AT2019vcb are consistent with the prompt radio-emitting TDE population. GSN 069, eRO-QPE2, and RxJ1302 are less variable than the majority of TDEs over time, although it is unclear how variable old radio emission from a synchrotron-emitting outflow would be long after the TDE occurred.

In Figure 7 (middle), we plot the 5–6 GHz variability index distribution of the radio sources calculated using Equation (5), X-ray

selected TDEs from Goodwin et al. (2022), and optically selected TDEs from Cendes et al. (2024). A KS test comparing the two TDE populations with the QPE sources returns a test statistic of 0.5/0.5 with p -value of 0.3/0.4 for the X-ray/optical TDE comparisons, respectively. Therefore, the distribution of the variability statistic of the QPE source sample is not statistically significantly different to either of the TDE samples.

The radio spectral indices of the QPE sources are consistent with an optically thin synchrotron-emitting source, except AT2019qiz (Section 3). The radio spectral indices of the QPE sources are also entirely consistent with the radio spectral indices of the X-ray selected TDE sample presented in Goodwin et al. (2025), which found spectral indices from $\alpha \approx -0.5$ to $\alpha \approx -1.5$ for 11 TDEs. In the case of an old, optically thin synchrotron-emitting source with an electron energy index, p of 2.7 (as observed for TDEs, e.g. Cendes et al. 2021), given the Granot & Sari (2002) synchrotron spectral model in which the characteristic minimum frequency (ν_m), self-absorption frequency (ν_a) and cooling frequency (ν_c) are ordered $\nu_m < \nu_a < \nu_c$, the spectral index could be either $-p/2 = -1.25$ (if the observing frequency is above the cooling break) or $(1 - p)/2 = -0.85$ (if the observing frequency is below the cooling break). The spectral indices of the radio emission from eRO-QPE2, GSN 069, and RxJ1302 of -0.6 to -0.9 are consistent with optically thin synchrotron emission in which the cooling break is above the observed frequency band. Although, given the age of the QPE sources are as large as > 10 yr, it is surprising that the radio spectra do not indicate a steepening due to the cooling break. The synchrotron cooling break evolves with $\nu_c(t) \propto t^{-1/2}$ (Granot & Sari 2002). A cooling break was observed in the radio spectrum of the TDE AT2019dsg at 25 GHz at 83 d post-TDE (Cendes et al. 2021) and 19 GHz at 132 d post-TDE for the TDE ASASSN-19bt (Christy et al. 2024). If the cooling break location continues to evolve with time and in the scenario in which the location of the cooling break at time post-TDE is similar for all TDEs, for the cooling break to be above the observed frequency of 5–6 GHz, the outflow must be $\lesssim 250$ d old. Such a small age can be ruled out for RxJ1302, GSN 069, and eRO-QPE2 as QPEs have been observed in these systems for

longer. However, we note that the radio spectra available for GSN 069 and eRO-QPE2 are limited in coverage and the synchrotron electron index p may be lower than $p = 2.7$ which would result in a less steep spectral index than calculated. Overall, the radio spectra observed for the QPE sources are consistent with radio spectra of TDEs.

Curiously, Kosec et al. (2025) recently reported the detection of a 1 700–2 900 km/s ionised outflow via X-ray absorption features in observations of GSN 069. They constrain the outflow distance to be $\approx 2 - 9 \times 10^{16}$ cm from the SMBH and do not find any ionised line emission during the QPEs, deducing that the outflow may be linked to recent transient activity in the galaxy nucleus, not to the QPEs themselves. The outflow is similar, although significantly faster, to outflows observed in TDEs such as ASASSN-14li (Miller et al. 2015) and ASASSN-20qc (Kosec et al. 2023). The outflow in GSN 069 appears to be stable on very long timescales, unlike the outflow recently detected in ZTF19acknsky (Chakraborty et al. 2025a), which is clearly associated with the QPEs themselves. Kosec et al. (2025) infer that the ionised outflow in GSN 069 has kinetic power $\dot{E} \sim 7 \times 10^{-39} - 2 \times 10^{41}$ erg/s from a continuously launched outflow with mass outflow rate $3 \times 10^{-3} - 8 \times 10^{-2} M_{\odot}$ yr. They deduce that the outflow cannot be a remnant outflow from previous SMBH activity, being at just 0.03 pc from the SMBH and instead conclude the outflow is likely linked to the recent transient activity in GSN 069 that has been ongoing since 2010. The energy, location, and velocity of this outflow are very similar to constraints obtained on outflows from TDEs in the radio (e.g. Cendes et al. 2024), and synchrotron emission from a shock between this outflow and the circumnuclear medium could produce the radio luminosity of GSN 069 of $\approx 2.5 \times 10^{36}$ erg/s. More broadly, this kind of compact (~ 0.03 pc), persistent outflow observed in X-ray for GSN 069 is consistent with the radio emission seen in all five radio-detected QPE sources, implying that low-level persistent outflows may be common among QPEs and linked to the underlying transient activity that creates the discs observed in these systems, such as a TDE.

5.3 Theoretical implications of radio properties for the QPE mechanism

The lack of strong radio emission in any of the QPE sources and the apparent lack of radio variability associated with the X-ray flares implies that the eruptions themselves do not produce strong outflows or jets.

5.3.1 Star-disc collision model

In the EMRI scenario, current models estimate $\sim 10^{-5} M_{\odot}$ of material is ejected during each disc collision (e.g. Yao et al. 2025), with a velocity v_{launch} given by:

$$v_{\text{launch}} = c \sqrt{\frac{R_g}{R_{\text{collision}}}} \quad (6)$$

where R_g is the gravitational radius of the SMBH and $R_{\text{collision}}$ the radius at which the object collides with the disc. Chakraborty et al. (2025b) detected rapidly varying absorption features in ZTF19acknsky associated with blueshifted emission corresponding to $v_{\text{out}} \sim 6 - 40\%$ c , consistent with $R_{\text{collision}}$ of 2.5–15 R_g for a $10^6 M_{\odot}$ SMBH. The outflow would then propagate freely until it encounters circumnuclear gas which may produce a shock that would emit synchrotron radiation. If we assume the radius at which this shock occurs is R_{shock} , then the velocity of the outflow

at which time the shock occurs is

$$v_{\text{shock}} = c \sqrt{\frac{R_g}{R_{\text{shock}}}} \quad (7)$$

For a $10^6 M_{\odot}$ SMBH and a shock radius of $\sim 10^{16}$ cm (typical of early TDE outflow emission e.g. Alexander et al. 2016; Goodwin et al. 2022), we find $v_{\text{shock}} \sim 0.005 c$. Assuming there is $m_{\text{ej}} \sim 10^{-5} M_{\odot}$ mass in the outflow with velocity $0.005 c$, such an outflow would have energy $E = \frac{1}{2} m_{\text{ej}} v_{\text{shock}}^2 \sim 10^{44}$ erg. This energy is many orders of magnitude smaller than typical outflow energies derived for TDEs of $10^{49} - 10^{51}$ erg (e.g. Goodwin et al. 2025; Cendes et al. 2024) and would not produce synchrotron emission with sufficient radio luminosity to detect, even in the case of an extremely dense circumnuclear medium or strong magnetic field. Therefore, the lack of variable radio emission detected correlated with the X-ray QPEs is consistent with the outflows expected in the disc collision model.

5.3.2 Disc instability model

In the disc instability model for QPEs, the X-ray flares are suggested to be produced by instability cycles where the QPEs are caused by magnetically driven outflows (e.g. Pan et al. 2022; Pan, Li, & Cao 2023). It is unclear in this scenario if episodic jet activity from each accretion event would be expected or detectable, as this would depend on the accretion rate, efficiency, and mass accreted during each instability event. However, the radio properties of QPEs observed to date would suggest that such instabilities do not result in significant outflows or jets, which one may expect if the instabilities trigger short- and low-mass accretion events onto the SMBH.

6. Summary

In this work, we present a comprehensive analysis of the radio properties of the 12 known QPE sources. Overall we find weak, compact radio emission coincident with 5/12 of the QPE sources. We find no correlation between the radio luminosity and QPE flare properties such as recurrence time, duration, and total energy radiated or the host galaxy properties such as SMBH mass, galaxy mass, or star formation rate. The radio-detected QPE sources are compact < 2.3 kpc, localised to the centre of their host galaxies, and faint ($\nu L_{\nu} \sim 5 \times 10^{36} - 5 \times 10^{38}$ erg/s). The radio spectra are optically thin (except AT2019qiz which shows a young radio-emitting outflow likely produced by the optically detected TDE), with spectral indices consistent with AGN or TDE populations. The compactness of the radio sources and lack of correlation between radio luminosity and SMBH mass is very unusual for AGN, suggesting the radio sources may instead to be linked to more exotic transient activity in the nuclei of the galaxies, such as a relatively recent TDE. The radio spectra and luminosities of the QPE sources are broadly consistent with observed radio emission from TDEs, although the lack of a long-term radio decay in GSN 069 is unexpected for an ageing TDE outflow. Future radio observations of a larger sample of QPEs will determine if compact, weak radio sources are common among the population of QPE sources and may provide further insight into the mechanism driving the radio emission observed in the current sample.

Supplementary material. The supplementary material for this article can be found at <https://doi.org/10.1017/pasa.2025.10083>.

Acknowledgements. A.J.G. thanks Andrew Mummery for contributing to Figure 4. A.J.G. is grateful for support from the Forrest Research Foundation. G.M. acknowledges MICIU/AEI/10.13039/501100011033 for support through grants n. PID2020-115325GB-C31 and PID2023-147338NB-C21. R.A. was supported by NASA through the NASA Hubble Fellowship grant #HST-HF2-51499.001-A awarded by the Space Telescope Science Institute, which is operated by the Association of Universities for Research in Astronomy, Incorporated, under NASA contract NAS5-26555.

The Australia Telescope Compact Array is part of the Australia Telescope National Facility (grid.421683.a) which is funded by the Australian Government for operation as a National Facility managed by CSIRO. We acknowledge the Gomeri people as the traditional owners of the Observatory site. The National Radio Astronomy Observatory is a facility of the National Science Foundation operated under cooperative agreement by Associated Universities, Inc.

References

- Alexander, K. D., Berger, E., Guillochon, J., Zauderer, B. A., & Williams, P. K. G. 2016, *ApJ*, **819**, L25
- Alexander, K. D., van Velzen, S., Horesh, A., & Zauderer, B. A. 2020, *SSR*, **216**, 81
- Anderson, J. M., & Ulvestad, J. S. 2005, *ApJ*, **627**, 674
- Arcodia, R., et al. 2021, *Natur*, **592**, 704
- Arcodia, R., et al. 2022, *A&A*, **662**, A49
- Arcodia, R., et al. 2024a, *A&A*, **684**, A64
- Arcodia, R., et al. 2024b, *A&A*, **690**, A80
- Arcodia, R., et al. 2025, arXiv e-prints, [arXiv:2506.17138](https://arxiv.org/abs/2506.17138)
- Barniol Duran, R., Nakar, E., & Piran, T. 2013, *ApJ*, **772**, 78
- Best, P. N., et al. 2005, *MNRAS*, **362**, 25
- Bykov, S. D., Gilfanov, M. R., Sunyaev, R. A., & Medvedev, P. S. 2025, *MNRAS*, **540**, 30
- CASA Team, et al. 2022, *PASP*, **134**, 114501
- Cendes, Y., Berger, E., Alexander, K., Laskar, T., & Goodwin, A. 2024, *ATel*, **16650**, 1
- Cendes, Y., et al. 2021, *ApJ*, **919**, 127
- Cendes, Y., et al. 2022, *ApJ*, **938**, 28
- Chakraborty, J., et al. 2021, *ApJ*, **921**, L40
- Chakraborty, J., et al. 2024, *ApJ*, **965**, 12
- Chakraborty, J., et al. 2025a, *ApJ*, **983**, L39
- Chakraborty, J., et al. 2025b, *ApJ*, **984**, 124
- Christy, C. T., et al. 2024, *ApJ*, **974**, 18
- Dey, A., et al. 2019, *AJ*, **157**, 168
- Franchini, A., et al. 2023, *A&A*, **675**, A100
- Giustini, M., Miniutti, G., & Saxton, R. D. 2020, *A&A*, **636**, L2
- Giustini, M., et al. 2024, *A&A*, **692**, A15
- Goodwin, A. J., et al. 2022, *MNRAS*, **511**, 5328
- Goodwin, A. J., et al. 2023a, *MNRAS*, **522**, 5084
- Goodwin, A. J., et al. 2023b, *MNRAS*, **518**, 847
- Goodwin, A. J., et al. 2024, *MNRAS*, **528**, 7123
- Goodwin, A. J., et al. 2025, arXiv e-prints, [arXiv:2504.08426](https://arxiv.org/abs/2504.08426)
- Granot, J., & Sari, R. 2002, *ApJ*, **568**, 820
- Hernández-García, L., et al. 2025, *NatAs*, [arXiv:2504.07169](https://arxiv.org/abs/2504.07169)
- Ho, L. C., & Ulvestad, J. S. 2001, *ApJS*, **133**, 77
- Hovatta, T., et al. 2008, *A&A*, **485**, 51
- Kaur, K., Stone, N. C., & Gilbaum, S. 2023, *MNRAS*, **524**, 1269
- King, A. 2020, *MNRAS*, **493**, L120
- Kosec, P., Pasham, D., Kara, E., & Tombesi, F. 2023, *ApJ*, **954**, 170
- Kosec, P., et al. 2025, *ApJ*, **978**, 10
- Lacy, M., et al. 2020, *PASP*, **132**, 035001
- Linial, I., & Metzger, B. D. 2023, *ApJ*, **957**, 34
- Linial, I., & Sari, R. 2023, *ApJ*, **945**, 86
- Lu, W., & Quataert, E. 2023, *MNRAS*, **524**, 6247
- McConnell, D., et al. 2020, *PASA*, **37**, e048
- Miller, J. M., et al. 2015, *Natur*, **526**, 542
- Miniutti, G., et al. 2023, *A&A*, **670**, A93
- Miniutti, G., et al. 2019, *Natur*, **573**, 381
- Miniutti, G., et al. 2025, *A&A*, **693**, A179
- Mummery, A. 2025, arXiv e-prints, [arXiv:2504.21456](https://arxiv.org/abs/2504.21456)
- Murphy, E. J., et al. 2011, *ApJ*, **737**, 67
- Newsome, M., et al. 2024, *ApJ*, **977**, 258
- Nicholl, M., et al. 2024, *Natur*, **634**, 804
- Pan, X., Li, S.-L., & Cao, X. 2023, *ApJ*, **952**, 32
- Pan, X., Li, S.-L., Cao, X., Miniutti, G., & Gu, M. 2022, *ApJ*, **928**, L18
- Pasham, D. R., et al. 2023, *NatAs*, **7**, 88
- Quintin, E., et al. 2023, *A&A*, **675**, A152
- Raj, A., & Nixon, C. J. 2021, *ApJ*, **909**, 82
- Sánchez-Sáez, P., et al. 2024, *A&A*, **688**, A157
- Shu, X. W., et al. 2017, *ApJ*, **837**, 3
- Sniegowska, M., Czerny, B., Bon, E., & Bon, N. 2020, *A&A*, **641**, A167
- Suková, P., Zajaček, M., Witzany, V., & Karas, V. 2021, *ApJ*, **917**, 43
- van Velzen, S., et al. 2016, *Sci*, **351**, 62
- Wang, M., Yin, J., Ma, Y., & Wu, Q. 2022, *ApJ*, **933**, 225
- Wevers, T., Pasham, D. R., Jalan, P., Rakshit, S., & Arcodia, R. 2022, *A&A*, **659**, L2
- Wevers, T., et al. 2019, *MNRAS*, **488**, 4816
- Wevers, T., et al. 2024, *ApJ*, **970**, L23
- Yang, L., et al. 2022, *ApJ*, **935**, 115
- Yao, P. Z., Quataert, E., Jiang, Y.-F., Lu, W., & White, C. J. 2025, *ApJ*, **978**, 91
- Zauderer, B. A., et al. 2011, *Natur*, **476**, 425
- Zhao, Z. Y., Wang, Y. Y., Zou, Y. C., Wang, F. Y., & Dai, Z. G. 2022, *A&A*, **661**, A55

Appendix A. ATCA radio observations of eRO-QPE2

The first ATCA radio observation of eRO-QPE2 was taken with the ATCA in compact H214 configuration, resulting in a low image resolution. There are two nearby sources which eRO-QPE2 is confused with in the compact configuration observation, resulting in a higher flux density measured for the target radio source. The second ATCA observation was taken in the extended 6 km configuration with a much higher image resolution. In Figure A1, we plot the optical image of the field with radio contours from both of the ATCA observations. It is clear that only in the second ATCA observation are the sources not confused. We therefore caution readers from interpreting the change in flux density between the two ATCA epochs as intrinsic source variability. A

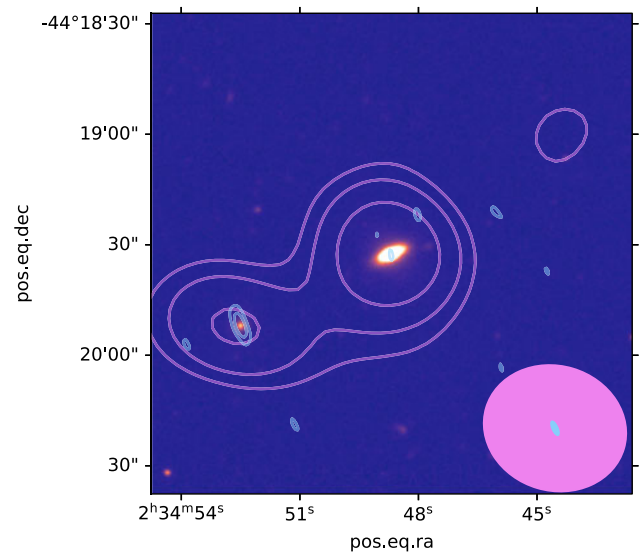


Figure A1. The DESI Legacy DR8 optical image of 2MASX J02344872-4419325, the host galaxy of eRO-QPE2, and the ATCA 5.5 GHz radio contours overlaid. The pink contours show the lower resolution ATCA observations from June 2022, whereas the blue contours show the higher resolution ATCA observations from December 2022. The size of the beam for each radio observation is plotted in the bottom right corner indicating the nominal image resolution.